Preliminary evaluation of the up-conversion emission of Y_2O_3:Er-Yb thin films prepared by a solid state photochemical deposition method

G. Cabello-Guzmán[a],*, Diego González[a], C. Caro-Díaz[a], L. Lillo-Arroyo[a], F. Valenzuela-Melgarejo[a], G. Cárdenas Triviño[b], G.E. Buono-Core[c], B. Chornik[d], Yosselin Huentupil[e]

[a] *Departamento de Ciencias Básicas, Facultad de Ciencias, Universidad del Bío-Bío, Chillán, Chile*
[b] *Facultad de Ingeniería, DIMAD, Centro de Biomateriales y Nanotecnología, Universidad del Bío-Bío, Concepción, Chile*
[c] *Instituto de Química, Pontificia Universidad Católica de Valparaíso, Valparaíso, Chile*
[d] *Deparamento de Física, Facultad de Ciencias Físicas y Matemáticas, Universidad de Chile, Santiago 8370415, Chile*
[e] *Facultad de Ciencias Químicas, Universidad de Concepción, Concepción, Chile*

ARTICLE INFO

ABSTRACT

Y_2O_3 thin films doped with different concentrations of erbium ions and co-doped with 10 mol% of ytterbium were synthesized by a solid state photochemical deposition method followed by a subsequent calcination process. The photo-reactivity of the thin films was monitored by Fourier transform infrared (FT-IR) spectroscopy. X-ray diffraction (XRD), X-ray photoelectron spectroscopy (XPS), scanning electron microscopy (SEM), UV–vis spectroscopy and photo-luminescence (PL) were employed to characterize the samples. The results reveal that Y_2O_3:Er films under 980 nm irradiation exhibit characteristic up-conversion emissions that are focused in the green region of the spectrum; these emissions are assigned to the $(^2H_{11/2}, {}^4S_{3/2}) \rightarrow {}^4I_{15/2}$ transitions of the Er^{3+} ions. These emissions greatly increase in intensity with the addition of Yb^{3+} ions in the preparation of the co-doped films. This phenomenon is explained based on the efficient $Yb^{3+} \rightarrow Er^{3+}$ energy transfer processes.

1. Introduction

The synthesis of inorganic nano/microstructures with novel chemical and physical properties has stimulated considerable attention due to their potential applications in diverse fields. Currently, several efforts have been made to explore novel approaches for preparing inorganic compounds to enhance their performance in existing applications [1]. Lanthanide oxides, such as, as functional materials have been extensively analyzed due to their outstanding optical, photo-catalytic and electronic properties [2]. Some characteristics of the Y_2O_3 metal oxide are summarized in Table 1.

The low phonon frequency shown by certain materials stimulates the up-conversion emission processes [5,6], and a wide band gap provides discrete energy levels between the conduction and valence bands of the host material for a wide variety of lanthanide (Ln^{III}) ions to act as activators [7]. Both properties are relevant in the design of luminescent materials.

Erbium ion-doping in various matrices has attracted much attention due to its diverse optical applications. Erbium ions as activators can convert infrared radiation into visible light, which is a phenomenon known as an up-conversion process [1]. However, the main feature of

erbium ions is the near-infrared (NIR) emission at 1540 nm corresponding to the $^4I_{13/2} \rightarrow {}^4I_{15/2}$ transition in the telecommunication window [2]. Independent of the type of erbium emission signals, its emissions are often very weak [8], which is a characteristic that is disadvantageous for its optical applications. Various authors [9] have adopted the introduction of a co-doping between two different Ln^{III} ions to enhance the luminescence intensity. One the of Ln^{III} ions acts as an absorber, and the other acts as an emitter with the purpose of using the energy transfer between both Ln^{III} ions to stimulate the up-conversion process. The up-conversion emissions are a characteristic of an emerging class of luminescent materials that convert lower-energy photons into higher-energy photons. For example, the introduction of these nano-structured materials into biological samples takes advantage of the fact that their incidence of NIR light in the range of 700–900 nm can pass through the biological sample without producing alterations, causing the excitation of the introduced material in its emission in the visible spectrum range (450–650 nm). This kind of optical phenomenon has several applications such as bio-labels, bio-sensing, bio-imaging and whole body photo-luminescent imaging in the biomedical field [10].

Many methods for the synthesis of Y_2O_3 doped with Ln^{III} ions have been proposed, including the solution combustion method [11], the sol-

Table 1
Optical properties of Y_2O_3.

Metal oxide/ properties	Spectral range of transparency	Optical band gap	Phonon frequency	Ref.
Y_2O_3	200–8000 nm	5.8–6.0 eV	380 cm^{-1}	[3,4]

gel technique [12], hydrothermal synthesis [13] and the precipitation method [14]. Among these methods, photochemical methods emerge as an alternative in the synthesis of inorganic materials due to their low cost, relatively simple implementation and mild conditions. Photochemical methods are different from other synthesis methods because they are selective. This selectivity occurs because the light absorption features of the reactants determine their reaction products [15]. For this reason, the application of photochemical methods as a synthesis technique has not been generalized because an essential requirement for a successful photo-deposition is the appropriate photo-reactivity of the precursor species under UV illumination.

In recent years, photochemical deposition methods have been proposed based on the use of UV light for the preparation of thin films or nanoparticles of a wide range of metals and ceramic materials. Some of these methods and their characteristics are summarized in Table 2.

In general, the photo-deposition process occurs when the precursor is photo-excited by the absorption of light to produce the photo-reduction of the metallic species that is deposited on the substrate surface [16].

In recent years, our group has focused on applying the photochemical metal organic deposition (PMOD) method for the preparation of mixed oxides such as perovskites [33] and spinels [34] doped with Ln^{III} ions to study their luminescent properties. This method was developed as a photolithographic deposition method to deposit metal oxide materials [35,36], without the use of photoresists, in ambient conditions, requiring no thermal of high vacuum processing. Subsequently, this technique has been used in the deposition of catalyst [30], electrical devices [31,37], gas sensors [32,38], magnetic materials [39] and optical materials [40]. The versatility of this methodology has allowed its use in the deposition of a wide range of materials and has attracted much attention because the experimental procedure is easy to handle, does not require sophisticated implementation and does not demand greater energetic cost. This technique is also known as the solid state photochemical deposition method, and it consists of the use of β-diketonate complexes as the precursor material. These complexes are dissolved in organic solvents and deposited on silicon or quartz substrates using the spin-coating technique. The film generated from the precursor complex is exposed to a set of UV lamps, resulting in the release of the ligand and the deposition of the reduced metal ion on the substrate. The metal ion is gradually oxidized under aerated conditions to generate a metal oxide thin film. In many cases, these films are amorphous oxides; therefore, a subsequent heat treatment is required to obtain crystalline films.

In this article, we focus on the use of β-diketonate complexes of Y (III) for the photo-deposition of Y_2O_3 films and the use of β-diketonate complexes of Er(III) and Yb(III) for the photo-deposition of Y_2O_3:Er-Yb to study their luminescent properties as up-conversion materials.

2. Experimental details

2.1. Preparation of amorphous thin films

For the deposition of Y_2O_3 films, the precursor complex yttrium(III) tris(2,2,6,6-tetramethyl-3,5-heptanedionate) [$Y(tmhd)_3$] was purchased from Aldrich Chemical Company. The substrates for film deposition were quartz plates (2×2 cm^2) and n- and p-type silicon (100) wafers (1×1 cm^2), which were obtained from Wafer World Inc., Florida, USA.

The $Y(tmhd)_3$ complexes were homogenized in a CH_2Cl_2 solution. The thin films were prepared as follows. A silicon chip was placed on a spin-coater and rotated at a speed of 600 rpm. An aliquot (0.5 ml) of the precursor complex in CH_2Cl_2 solution was deposited onto the silicon chip and allowed to spread. The spin-coater motor was stopped after 30 s, and a thin film of the complex remained on the chip. The quality of the films was examined using optical microscopy (500x magnification).

For the deposition of Y_2O_3:xEr-Yb films, solutions of $Y(tmhd)_3$ with different proportions of $Er(tmhd)_3$ (where x = 5, 10 and 15 mol%) and 10 mol% of $Yb(FOD)_3$ were spin-coated on the appropriate substrate, and the thin films were irradiated until no absorption due to the complexes was observed in the infrared spectrum.

2.2. Photolysis of the complexes as films on Si(100) surfaces

All photolysis experiments were performed following identical procedures. First, the Fourier transform infrared spectroscopy (FT-IR) spectrum of the starting film was obtained. Then, the chip was placed under a UV-lamp setup that was equipped with two 254 nm 6 W tubes in air. The reaction progress was monitored by recording the FT-IR spectrum at different time intervals following a decrease in the IR absorption of the complexes. After the FT-IR spectrum showed no evidence of the starting material, the chip was rinsed several times with dry acetone to remove all remaining organic products on the surface prior to analysis. To obtain films with a specific thickness, successive layers of the precursor materials were deposited by spin-coating and irradiated as previously described. This process was repeated several times until the desired thickness was achieved. Post-annealing was performed under a continuous flow of synthetic air at different temperatures (350-950 °C) for 3 h in a programmable Lindberg tube furnace.

Table 2
List of some photochemical deposition methods.

| Method	Precursors	Examples
Photochemical deposition (PCD) technique	Ionic compounds such as $M_2(SO_4)_n$ and $Na_2S_2O_3$.	Particles and films of Cu_xS [17] Cu_xZn_yS [18] and SnO_2 [19]
Photochemical Synthesis	Metal salts such as MCl_n and $M(NO_3)_n$	Particles of As°, Sb°, Bi°, Pb°, Se°, Te° and Bi_4Te_3 Sb_xBi_{1-X} compounds [20], Ag nanoparticles [21]
Photodeposition from colloid solutions (PDCS)	Ionic compounds such as $ZnSO_3$, $CdSO_4$, and H_2SeO_3 Colloid chromophores: ZnS, CdS	Particles and films of metal oxides (ZnO, CdO) [22] and Se [23]
Photocatalytic deposition	Metallic ions in solution and semiconductors as supports (TiO_2, ZnO)	X-NPs/TiO_2 X = Au, Ag, Cu, Pt, NPs = nanoparticles [24–26]
Liquid phase photodeposition (LPPD)	β-diketonate metal complexes: $M(acac)_n$ and $M(tmhd)_n$	NiO nanoparticles [27], Pd [28], and Pt [29] nanoparticles
Photochemical metal organic deposition (PMOD)	β-diketonate, carboxylate and tropolonate complexes	FeO_X films [30], $PbZr_{0.52}Ti_{0.48}O_3$ films [31], and MoO_3 films [32]

2.3. Characterization of the thin films

The FT-IR spectra were obtained with a $4\,cm^{-1}$ resolution on a Perkin Elmer Spectrum Two FT-IR spectrophotometer. The UV spectra were obtained with a 1 nm resolution on a Perkin Elmer Model Lambda 25 UV–vis spectrophotometer. X-ray diffraction (XRD) patterns were obtained using a D8 Advance Bruker X-ray diffractometer; the X-ray source was Cu Kα radiation (40 kV/30 mA). X-ray photoelectron spectroscopy (XPS) was performed on an XPS-Auger Perkin Elmer electron spectrometer Model PHI 1257 that included an ultra-high vacuum chamber, a hemispherical electron energy analyzer and an X-ray source that provided unfiltered Kα radiation from its Al anode (hν = 1486.6 eV). The pressure of the main spectrometer chamber during data acquisition was maintained at approximately 10-7 Pa. The binding energy (BE) scale was calibrated using the peak of adventitious carbon, which was set to 284.6 eV. The accuracy of the BE scale was ± 0.1 eV. The morphology and presence of elements in the samples were evaluated by scanning electron microscopy (SEM) with a Hitachi model SU 3500 with an accelerating voltage of 10.0 kV. SEM was coupled with Bruker model Quantax 100 energy dispersive X-ray spectroscopy (EDX) for semi-quantitative determinations.

The up-conversion luminescent properties were determined with a Hitachi F-7000 fluorescent spectrometer using a power-tunable 980 nm diode laser. All measurements were performed at room temperature.

3. Results and discussion

3.1. Photo-reactivity of the precursor complexes

To evaluate the liquid-phase photochemistry, concentrations of each precursor complex ($\leq 10^{-5}$ mol/L) that were diluted in dichloromethane were exposed to a set of UV lamps (254 nm) to determine the spectral changes of the irradiated samples at different time intervals. Fig. 1 shows the optical absorption spectrum of each complex, with all of them exhibiting a single band at 276 nm corresponding to a π→π* electronic transition of a carbonyl group (C=O) of the ligand [41]. This same spectral absorption indicates that the ligands of each precursor complex are similar in terms of structure and functional groups. In the development of photolysis, a slight increase in the degree of absorption produced by the electronic excitation experienced by each precursor complex is observed at the beginning. Subsequently, with the
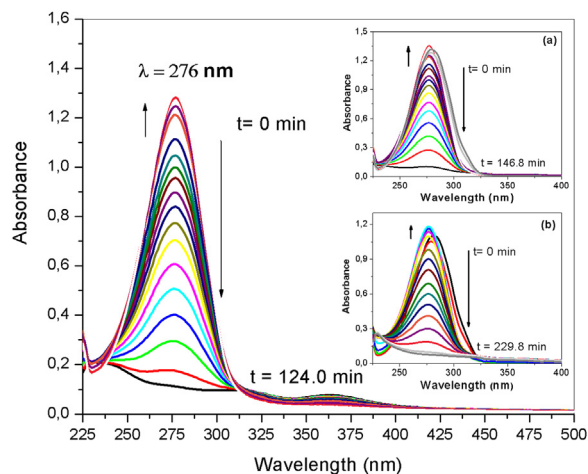
Fig. 1. Absorption spectral changes observed at room temperature of a solution of the Y(tmhd)₃ complex (3.16×10^{-5} mol/L) in CH₂Cl₂ upon 124 min of UV irradiation. Insets: **(a)** Er(tmhd)₃ complex (4.61×10^{-5} mol/L) after 146.8 min of UV irradiation, **(b)** Yb(FOD)₃ complex (2.26×10^{-6} mol/L) after 229.8 min of irradiation with 254 nm light. The arrows indicate the direction of the spectral evolution with time.

course of the UV radiation, a gradual decrease in the absorption bands is observed. After 124, 147 and 230 min of exposure for the Y(tmhd)₃, Er(tmhd)₃ and Yb(FOD)₃ complexes, respectively, all bands associated with the complexes were greatly diminished. No spectral evidence for the presence of intermediate species is found during the photolysis process. These spectral changes reflect the fragmentation of the precursor complexes, which results in the release of the metal ion and its photo-reduction. Similar observations have been reported with other types of β-diketonate complexes [42,43].

Films of the precursor complexes of Y(tmhd)₃ with different molar proportions of Er(tmhd)₃ and Yb(FOD)₃ were deposited on Si wafers by spin-coating, and they were irradiated in air with a 254 nm UV source. The FT-IR spectral changes associated with the solid state photolysis are shown in Fig. 2. At time zero (t = 0 h), an intense band at $2960\,cm^{-1}$ associated with the C-H vibration modes, bands at 1575–1504 and $1405–1352\,cm^{-1}$ associated with the antisymmetric and symmetric carbonyl group (C=O) and bands at $1224–1132\,cm^{-1}$ corresponding to C-O vibration modes are observed. The difference in energy between the antisymmetric and symmetric C=O stretching vibrations is indicative of the nature of the bonding mode of the β-diketonate ligands. The intensity of the bands associated with β-diketonate complexes gradually decreases with every 24 h of irradiation. After 144 h of exposure, all bands associated with the β-diketonate complexes are substantially diminished, and only a minimal intensity of bands attributed to by-products from the photo-degradation of the β-diketonate complexes are observed.

3.2. FT-IR and XRD characterization of the photo-deposited thin films

The photo-deposited samples were treated at different temperatures from 350 to 950 °C and preliminary examined by FT-IR, as shown in Fig. 3. The results show that for both samples (non-doped and co-doped) annealed at 350 °C, this temperature was not enough to remove the organic residues or to provide evidence for the formation of oxides. The signal located at 3380 or 3395 cm^{-1} is associated with the vibrational modes of hydroxyl groups (OH⁻), the band (doublet) located at 1508 and 1400 cm^{-1} can be attributed to carbonate formation (CO₃²⁻) [44,45], and finally, a weak signal at 845 cm^{-1} corresponds to the absorption of a small amount of CO₃²⁻ [46]. The films under these conditions most likely adopt a Y(OH)CO₃-type composition, and the bands attributed to O-H and CO₃²⁻ vibrations are due to moisture absorption during the measurement. These signals decrease significantly when the samples are annealed at 650 °C, and a new signal appears at ∼ 560 cm^{-1}, which corresponds the Y-O vibration mode in the formation of the metal oxide. Finally, when the samples are treated at 950 °C, three new peaks appear in the spectrum at 460, 560 and 1078 cm^{-1} that are associated with the Y-O stretching vibrations of the host lattice [46].

Fig. 4 shows the XRD results of the samples of the Y₂O₃ and Y₂O₃:Er-Yb thin films annealed at 950 °C, and both samples show similar patterns with two sharp and intense peaks corresponding to the (222) and (622) orientations located at 29.2° and 58.7°, respectively, of the cubic crystalline phase of Y₂O₃ [14]. However, the presence of some peaks assigned to the partial formation of hydroxylated species is observed. The incorporation of co-doping (Er and Yb) into the host lattice contributes to the reduction of secondary phases. To evaluate the degree of incorporation of an additive into the host lattice or the replacement of some of the ions of the crystal lattice by the introduction of the additive, slight shifts in the diffraction peaks with respect to the positions of the signals of the pure Y₂O₃ are used as evidence. The ionic radii of Er³⁺ and Yb³⁺ are 103 pm and 116 pm, respectively, which are similar to the ionic radius of the Y³⁺ ion (104 pm) in the host lattice. Therefore, a certain degree of substitution or incorporation of additives into the crystalline lattice is possible. The inset in Fig. 4(a) and (b) shows the variation of the peak positions of the (222) and (622) lattice planes, respectively.
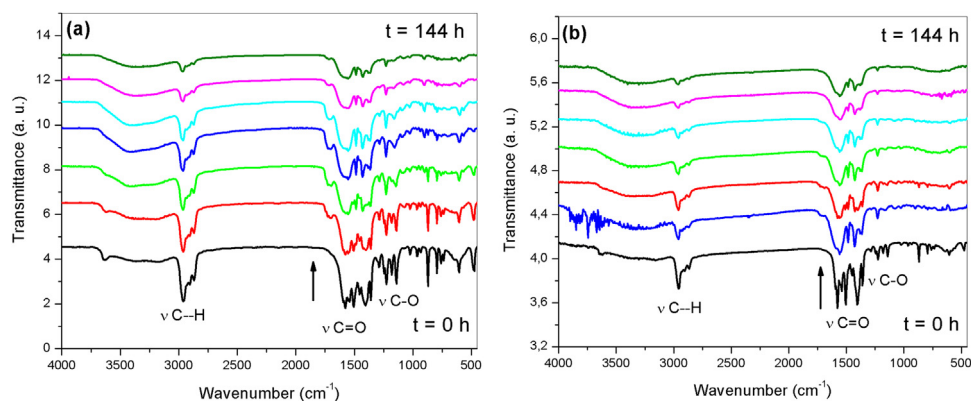
Fig. 2. FT-IR spectra of the following films on Si(100) wafers exposed to UV light for 0, 24, 48, 72, 96, 120 and 144 h: **(a)** Y(tmhd)$_3$ and **(b)** Y(tmhd)$_3$ with 10 mol% of Er(tmhd)3 and 10 mol% of Yb(FOD)$_3$ complexes.
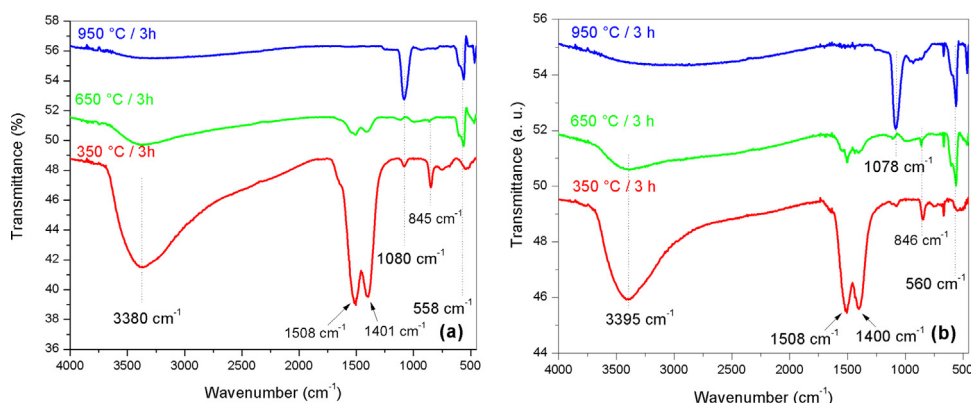

Fig. 3. FT-IR spectra for the photo-deposited films of **(a)** Y$_2$O$_3$ and **(b)** Y$_2$O$_3$:Er-Yb as a function of annealing temperature.
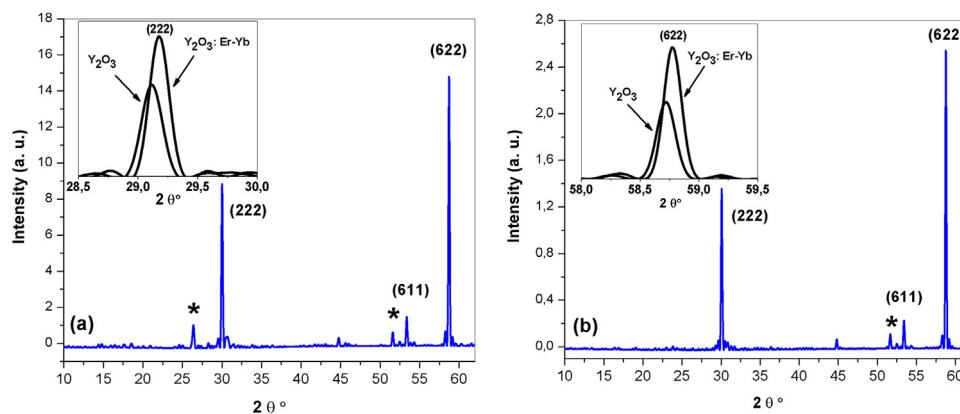

Fig. 4. XRD pattern of photo-deposited films **(a)** Y$_2$O$_3$ and **(b)** Y$_2$O$_3$:Er-Yb annealed in air at 950 °C for 3 h. The peaks labeled with (*) correspond to the formation of Y(OH)$_3$. The inset figures show the variation of the diffraction peaks corresponding to the (222) and (622) orientations, respectively.

3.3. XPS and SEM-EDS analysis of the photo-deposited films

The chemical composition of the Y$_2$O$_3$ films co-doped with Er and Yb annealed at 950 °C was analyzed by XPS. The Y 3d signal in the Y$_2$O$_3$ co-doped film (Fig. 5a) exhibits one doublet with binding energies at 158.4 and 160.5 eV corresponding to Y 3d$_{5/2}$ and Y 3d$_{3/2}$, respectively, and the separation between these contributions is 2.1 eV. These results are consistent with the formation Y$_2$O$_3$ [47,48].

The O 1s peak (Fig. 5b) consists of two types of contributions: one of them located at 529.7 eV (95.5%) defined as O$_{lat}$ corresponding to the lattice oxygen in the Y—O bond due to yttrium oxide formation [42], and the other contribution located at 532.0 eV (4.50%) defined as O$_{ads}$ attributable to the ionization of oxygen species adsorbed on the sample

surface [49].

The spectral regions corresponding to Er 4d and Yb 4d are observed at 168.7 eV and 185.2 eV, respectively, assigned to Er$_2$O$_3$ and Yb$_2$O$_3$ formation. These values are consistent with those reported by other authors [50,51].

The surface morphology and the elemental composition of the Y$_2$O$_3$ and Y$_2$O$_3$:Er-Yb films annealed at 950 °C are displayed in Figs. 6, 7. From the SEM images (Fig. 6(a)), we can see that the Y$_2$O$_3$ sample consists of a relatively uniform surface with some circular formations of different diameters belonging to the remaining solvent products of the photo-deposition step. The elemental mappings performed via EDS are shown in Fig. 6(b),(c),(d). As the mappings show, yttrium and oxygen are homogeneously and randomly distributed on the film surface, and
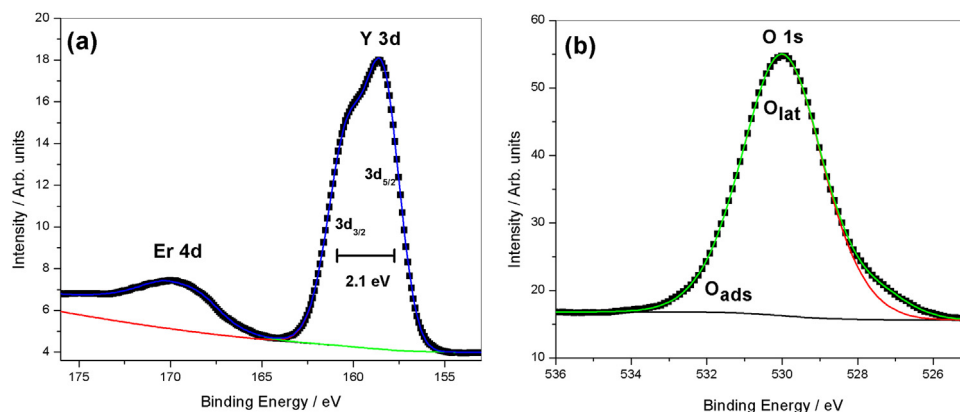
Fig. 5. XPS spectrum of **(a)** the Y 3d and Er 4d core levels and **(b)** O 1 s of the Y_2O_3:Er-Yb film annealed at 950 °C.
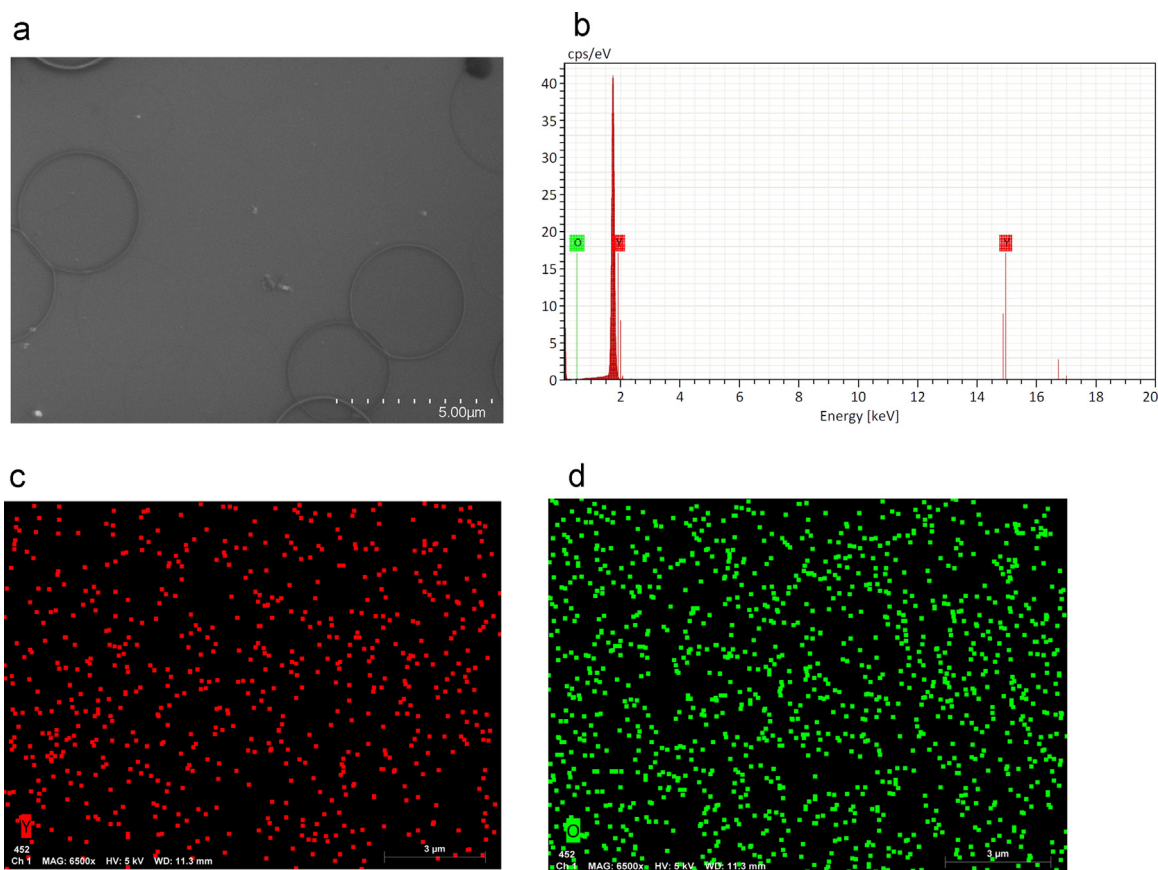

Fig. 6. SEM-EDS observation of the Y_2O_3 films annealed at 950 °C: **(a)** SEM image; **(b)** elemental composition from the EDS spectra; **(c)** elemental mapping of yttrium; and **(d)** elemental mapping of oxygen in the film.

their arrangement lacks compactness or agglomeration.

The morphology of the Y_2O_3:Er-Yb film is exhibited in Fig. 7(a), showing that the film consists of a smooth surface with some circular formations that represent a lesser proportion than that in the previous case. The distribution of elements by EDS (see Fig. 7(b)) shows the presence of each of the elements involved (Y, O, Er and Yb), and the elemental mappings (Fig. 7(c) and (d)) show that the additives are homogenously and randomly distributed on the film surface. The results of the main elemental composition of each of the samples are shown in Table 3. These values are close to the atom ratio in the stoichiometric composition of Y_2O_3. However, the O/Y ratio increases slightly in the co-doped samples due to the contribution to the oxidation reaction of each of the additives.

3.4. UV–visible spectra and band gap energy measurements of the films

The UV–vis transmittance spectra of the Y_2O_3 doped with different concentrations of erbium (expressed in mol%) were monitored in the range of 200–1000, nm and the obtained spectra are shown in Fig. 8(a). In general, the samples showed a low absorbance in the visible-NIR region, whereas the absorbance was high in the UV region. The spectrum in the UV region contained two absorption bands located at 210 and 240 nm attributed mainly to the charge transfer process of the host material and to transitions associated with extrinsic states, such as defect states, vacancies and impurities, respectively [52]. The slight decrease in transmittance along the spectrum results from the gradual increase in the dopant concentration. Fig. 8b shows the UV–vis transmittance spectra of pure, doped and co-doped Y_2O_3 films. For the co-
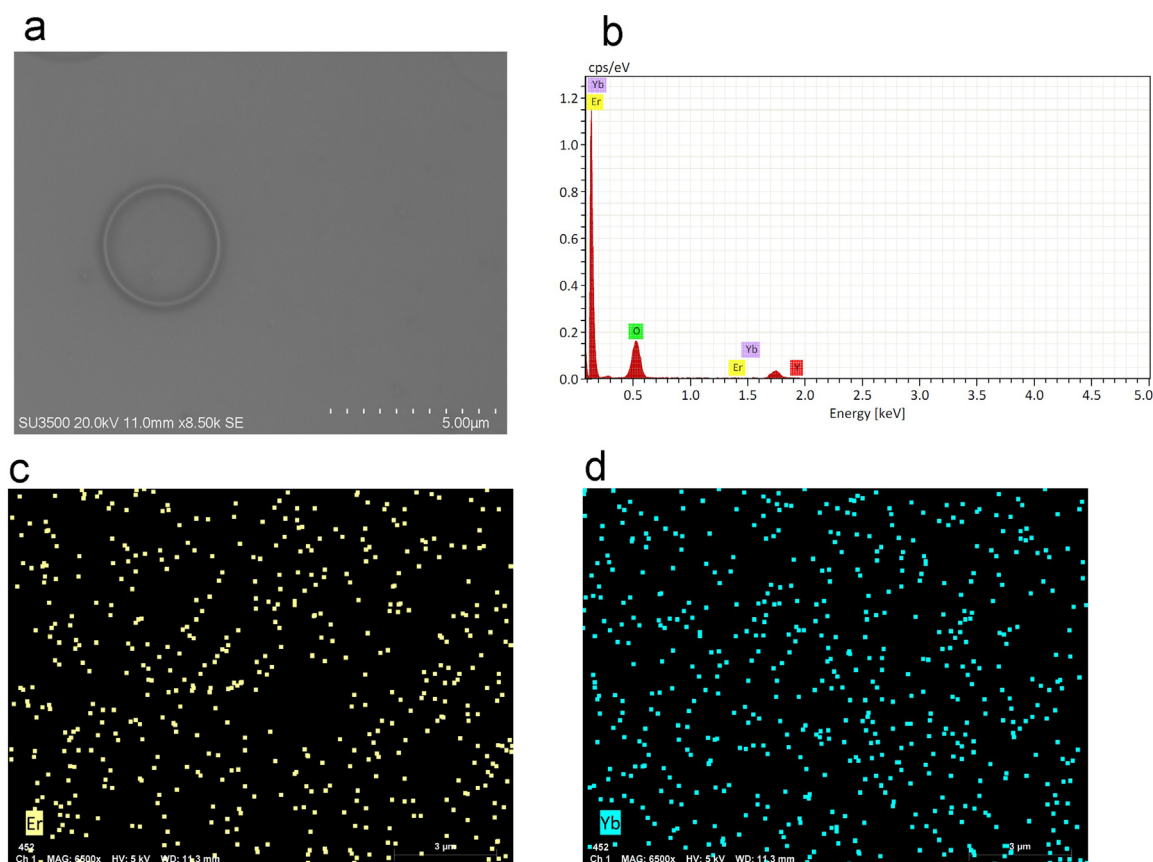
Fig. 7. SEM-EDS observation of the Y_2O_3:Er-Yb films annealed at 950 °C: **(a)** SEM image; **(b)** elemental composition from the EDS spectra; **(c)** elemental mapping of erbium; and **(d)** elemental mapping of ytterbium in the film.

Table 3
Percentage of each element obtained from the EDS analysis of the samples annealed at 950 °C.

Sample/element	O-K atom %	Y atom %	Er atom %	Yb atom %	O/Y (1.5)[a]
Y_2O_3	59.04	40.96	–	–	1.44
Y_2O_3:xEr-Yb	55.70	34.05	5.05	5.20	1.64

Observations: x = 10 mol% of Er and 10 mol% of Yb.
[a] corresponding to the theoretical value in the stoichiometry of Y_2O_3.

doped sample, an additional absorption band located at 308 nm is observed, which can be attributed to the charge transfer band of Yb^{3+}–O^{2-} or the effect of the 4f electrons of Yb^{3+} [53]. The optical band gap (E_g) of the pure, doped and co-doped Y_2O_3 thin films was calculated using the Tauc plot method [54] (shown in the inset of Fig. 8b). The E_g values obtained for the Y_2O_3, Y_2O_3:Er and Y_2O_3:Er-Yb thin films were 5.30 eV, 5.02 eV and 4.78 eV, respectively. The results show that the introduction of additives into the Y_2O_3 lattice produces energy levels in the energy gap between the conduction and valence bands (energy levels of donors or acceptors) that result in the slight decrease of the optical
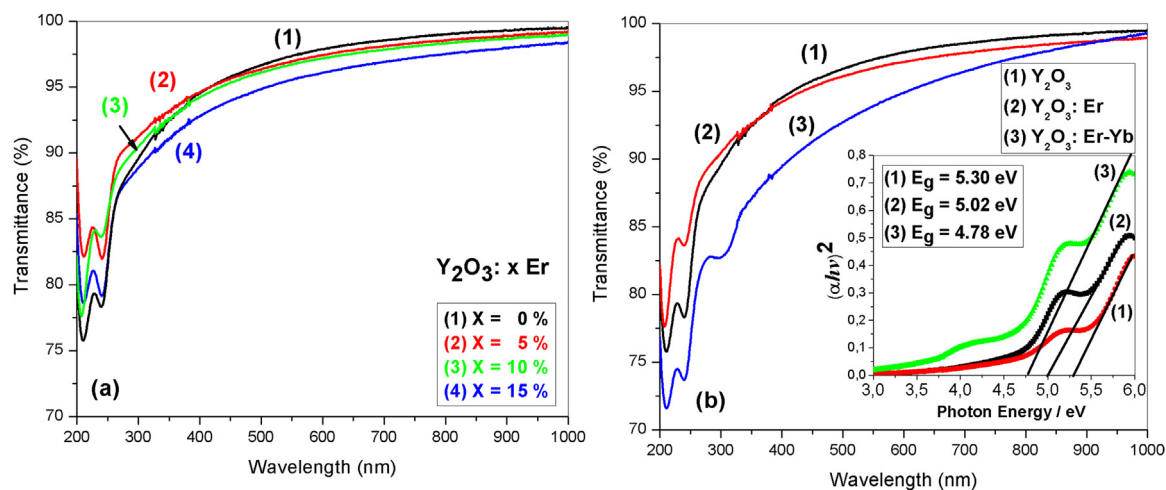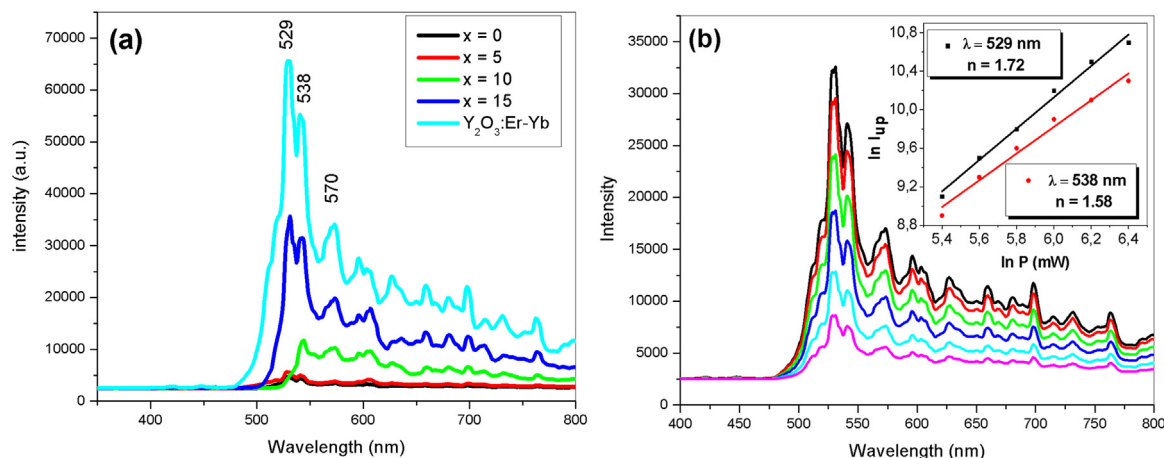

Fig. 8. Transmittance spectra for **(a)** Y_2O_3:xEr thin films with different concentrations of erbium as the additive, where x = 0, 5, 10, and 15 mol% of Er and **(b)** pure, doped and co-doped Y_2O_3 thin films. The inset shows the estimation of the optical band gap energy (Eg) of the pure, doped and co-doped samples.

Fig. 9. Up-conversion emission spectra of **(a)** Y_2O_3:xEr thin films with different concentrations of erbium as the additive, where x = 0, 5, 10, and 15 mol% of Er and Y_2O_3: Er-Yb thin films at 10 mol% of Er and 10 mol% of Yb. **(b)** The dependence of the up-conversion emissions at different excitation power levels. The inset shows plots of the natural logarithm of the emission intensity as a function of the natural logarithm of the excitation power at 529 and 538 nm emissions of the Y_2O_3:xEr films, where x = 15 mol%.
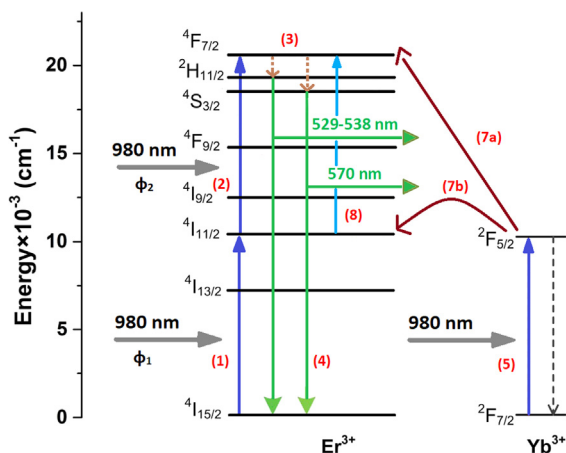
Fig. 10. Schematic energy level diagram showing the up-conversion mechanism of the Y_2O_3:Er and Y_2O_3:Er-Yb thin films.

band gap; in addition to this factor, the defects of the material as well as the oxygen vacancies also contribute to the formation of discrete energy levels. Thus, the optical band gap energy is very sensitive to the preparation method and the experimental parameters applied in the synthesis.

3.5. Evaluation of the luminescent properties of the films

Several studies [55–57] have reported the behavior of the up-conversion emissions from erbium ions as an additive in different matrices. It has been observed that under an excitation at 980 nm, a green emission occurs at 520–540 nm and another at 540–570 nm that are assigned to the radiative transitions $^2H_{11/2} \rightarrow {}^4I_{15/2}$ and $^4S_{3/2} \rightarrow {}^4I_{15/2}$, respectively, and a red emission at 640–690 nm corresponding to the radiative transition $^4F_{9/2} \rightarrow {}^4I_{15/2}$ of erbium ions.

Fig. 9(a) shows the up-conversion emission spectra of Y_2O_3 thin films doped with different concentrations of erbium under an excitation at 980 nm. The up-conversion spectra consist of an intense band centered at 529 and 538 nm and another of lower intensity at 570 nm originating from the $(^2H_{11/2}, {}^4S_{3/2}) \rightarrow {}^4I_{15/2}$, radiative transitions. In contrast, the red emission bands are very weak and cannot be clearly visualized. The lack of intensity or the absence of some emission bands in the visible spectrum has been documented by some authors [58]. These authors attributed this phenomenon to the differences in the

crystallinity, morphologies and the intrinsic defects of the material. In our case, the presence of some diffraction peaks corresponding to the (222) and (622) orientations demonstrate a specific crystalline orientation and the partial crystallization of our films after they were annealed at 950 °C. It is also likely that the formation of a small number of secondary phases according to the XRD results is determinant in the absence of some of the emissions in the visible spectrum. All these factors may influence the luminescence properties of the films.

The results reveal that the doping concentration influences the intensity of the emission; at low erbium concentrations (5 and 10 mol%), weak emission signals are observed, and the maximum emission intensity occurs at 15 mol% of Er. However, the co-doped samples (10 mol% of Er and 10 mol% of Yb) display a considerable increase in their emissions in the green region of the spectrum, and in this way, the energy transfer processes from ytterbium to erbium greatly contribute to their up-conversion emissions.

As one approach to understand the up-conversion emission mechanisms, we first determined the excitation power dependence of up-conversion emissions, given in Fig. 9b, and the number of photons required for the main emissions based on the following equation: $I_{up} \propto P^n$ where I_{up} is the up-conversion emission intensity, P is the pumping power, and n is the number of pumping photons required. The value of n can be obtained from the slope of the linear plots between ln (I_{up}) and ln(P) [59]. The calculated n values for the 529 and 538 nm emissions are 1.72 and 1.58, respectively, as shown in the inset of Fig. 9(b). Generally, a straight line with a slope of ~ 2 indicates that these emissions are correlated with a two-photon absorption process, which is responsible for the up-conversion emissions.

Based on our results, the possible up-conversion mechanisms for doped and co-doped samples are discussed based on the simplified energy level diagram shown in Fig. 10. In the doped samples, (1) the erbium ions in the $^4I_{15/2}$ ground state are pumped by one of the NIR laser photons to the $^4I_{11/2}$ state through ground state absorption (GSA), (2) the other NIR laser photon promotes the population stored in the $^4I_{11/2}$ level to the $^4F_{7/2}$ level via excited state absorption (ESA), (3) the excited erbium ions in the $^4F_{7/2}$ state decay non-radiatively and populate the $^2H_{11/2}$ and $^4S_{3/2}$ levels, and (4) the radiative relaxation from these $^2H_{11/2}$ and $^4S_{3/2}$ levels to the ground $^4I_{15/2}$ state gives emissions in the green region from 529 to 538 nm and 570 nm corresponding to the $^2H_{11/2} \rightarrow {}^4I_{15/2}$ and $^4S_{3/2} \rightarrow {}^4I_{15/2}$ transitions, respectively. In the co-doped samples, (5) the pumping light at 980 nm matches the $^2F_{7/2} \rightarrow {}^2F_{5/2}$ transition within the ytterbium ion. (6) After excitation, part of the population stored in the $^2F_{5/2}$ level relaxes non-radiatively to the ground $^2F_{7/2}$ state of the ytterbium ion, and (7) the other part of the

population stored in the $^2F_{5/2}$ level is promoted to the excited levels of the erbium ion by an energy transfer process (ET) that can be generated by two paths: (a) one of path involves the ET from the $^2F_{5/2}$ level (Yb^{3+}) to the $^4F_{7/2}$ level (Er^{3+}), which subsequently promotes steps (3) and (4) previously described; and (b) the other path is the ET from the $^2F_{5/2}$ level (Yb^{3+}) to the $^4I_{11/2}$ level (Er^{3+}) and (8) further excitation from the $^4I_{11/2}$ level (Er^{3+}) to $^4F_{7/2}$ (Er^{3+}) occurs after ET from the ytterbium ion in a second photon absorption, again stimulating steps (3) and (4). Thereby, the mechanism of energy transfer constitutes a decisive step in the up-conversion properties of the co-doped samples.

4. Conclusions

The photochemically active β-diketonate complexes of Y(III), Er(III) and Yb(III) were used as precursors in the preparation of Y_2O_3:Er and Y_2O_3:Er-Yb thin films, and these films were subjected to post-annealing at 950 °C. The results obtained via XRD, XPS and EDS showed the formation of Y_2O_3 and the presence of erbium and ytterbium in the co-doped films. The doped samples under 980 nm excitation showed up-conversion emissions from 529 to 538 nm and at 570 nm that were assigned to the ($^2H_{11/2}$, $^4S_{3/2}$)→$^4I_{15/2}$, energy level transitions of the Er^{3+} ions, corresponding to the green region of the spectrum. The absence of some signals in the visible spectrum was attributed to a partial crystallization of the films after they were thermally treated at 950 °C. The enhancement of the up-conversion emissions in the green region of the spectrum was observed in the co-doped samples due to the energy transfer from the Yb^{3+} to Er^{3+} ions. However, further studies are required to determine the detailed relationship between the up-conversion properties and the crystalline structure adopted by the material.

Acknowledgments

References

[1] Guogang Li, Chong Peng, Cuimiao Zhang, Zhenhe Xu, Mengmeng Shang, Dongmei Yang, Xiaojiao Kang, Wenxin Wang, Chunxia Li, Ziyong Cheng, Jun Lin, Inorg. Chem. 49 (2010) 10522–10535.

[2] N. Wang, J. Liu, W. Gu, Y. Song, F. Wang, ToWard Synergy Of Carbon And La$_2$O$_3$ in their hybrid as efficient catalyst for oxygen reduction reaction, RSC Adv. 6 (2016) 77786–77795.

[3] A.N. Meza-Rocha, E.F. Huerta, E. Zaleta-Alejandre, Z. Rivera-Alvarez, C. Falcony, Enhanced photoluminescence of Y$_2$O$_3$:Er^{3+} thin films by Li$^+$ co-doping, J. Lumin. 141 (2013) 173–176.

[4] E.J. Rubio, V.V. Atuchin, V.N. Kruchinin, L.D. Pokrovsky, I.P. Prosvirin, C.V. Ramana, Electronic structure and optical quality of nanocrystalline Y$_2$O$_3$ film surfaces and interfaces on Silicon, J. Phys. Chem. C 118 (2014) 13644–13651.

[5] Riya Dey, Vineet Kumar Rai, Yb^{3+} sensitized Er^{3+} doped La$_2$O$_3$ phosphor in temperature sensors and display devices, Dalton Trans. 43 (2014) 111–118.

[6] A. Siai, P. Haro-Gonzalez, K. Horchani-Naifer, M. Ferid, La$_2$O$_3$: Tm, Yb, Er upconverting nano-oxides for sub-tissue lifetime thermal sensing, Sens. Actuators B Chem. 234 (2016) 541–548.

[7] Liang Li, Xiyan Zhang, Zhaohui Bai, Weili Dong, Hui Shi, Qingxue Xue, Preparation and near-infrared luminescence properties of Y$_2$O$_3$:Er^{3+},Yb^{3+} nanopowders, Infrared Phys. Technol. 73 (2015) 49–53.

[8] A.N. Meza-Rocha, C. Canto, E. Andrade, O. De Lucio, E.F. Huerta, F. González, M.F. Rocha, C. Falcony, Visible and near infra-red luminescent emission from Y$_2$O$_3$:Er^{3+} films co-doped with Li$^+$ and their elemental composition by ion beam analysis, Ceram. Int. 40 (2014) 14647–14653.

[9] Lei Yin Ang, Meng Earn Lim, Li. Ching Ong, Yong Zhang, Applications of upconversion nanoparticles in imaging, detection and therapy, Nanomedicine 6 (2011) 1273–1288.

[10] Rajesh Adhikari, Applications of upconversion nanoparticles in nanomedicine, Nanomed. Nanotechnol. 7 (4) (2016) e141.

[11] C. Joshi, A. Dwivedi, S.B. Rai, Structural morphology, upconversion luminescence and optical thermometric sensing behavior of Y$_2$O$_3$:Er^{3+}/Yb^{3+} nano-crystalline phosphor, Spectrochim. Acta A 129 (2014) 451–456.

[12] James A. Dorman, Ju.H. Choi, Gregory Kuzmanich, Jane P. Chang, Elucidating the

[13] effects of a rare-earth oxide shell on the luminescence dynamics of Er^{3+}:Y$_2$O$_3$ nanoparticles, J. Phys. Chem. C 116 (2012) 10333–10340.

[13] Yuanbing Mao, Jian Y. Huang, Roman Ostroumov, Kang L. Wang, Jane P. Chang, Synthesis and luminescence properties of Erbium-doped Y$_2$O$_3$ nanotubes, J. Phys. Chem. C 112 (2008) 2278–2285.

[14] T. López-Luke, E. De la Rosa, I. Campos Villalobos, R.A. Rodriguez, C. Ángles-Chávez, P. Salas, Damon A. Wheeler, J.Z. Zhang, Improving pure red upconversion emission of Co-doped Y$_2$O$_3$:Yb^{3+}–Er^{3+} nanocrystals with a combination of sodium sulfide and surfactant Pluronic-F127, J. Lumin. 145 (2014) 292–298.

[15] Xinsheng Liu, Inorganic photochemical synthesis, in: Ruren Xu, Yan Xu (Eds.), Modern Inorganic Synthetic Chemistry, Elsevier, 2011, pp. 129–150.

[16] J.L. Rodriguez, M.A. Valenzuela, F. Pola, H. Tiznado, T. Poznyak, Photodeposition of Ni nanoparticles on TiO$_2$ and their application in the catalytic ozonation of 2,4-dichlorophenoxyacetic acid, J. Mol. Catal. A: Chem. 353–354 (2012) 29–36.

[17] R. Suriakarthick, V. Nirmal Kumar, T.S. Shyju, R. Gopalakrishnan, Investigation on post annealed copper sulfide thin films from photochemical deposition technique, Mater. Sci. Semicond. Process 26 (2014) 155–161.

[18] Masaya Ichimura, Yosuke Maeda, Conduction type of nonstoichiometric alloy semiconductor Cu$_x$Zn$_y$S deposited by the photochemical deposition method, Thin Solid Films 594 (2015) 277–281.

[19] A. Dengbaoleer, Masaya Ichimura, UV irradiation effects on hydrogen sensors based on SnO$_2$ thin films fabricated by the photochemical deposition, Solid-State Electron 69 (2012) 1–3.

[20] A. Luz, A. Malek-Luz, C. Feldmann, Photochemical synthesis of particulate main-group elements and compounds, Chem. Mater. 25 (2013) 202–209.

[21] Hongxia Yu, Qiao Zhang, Hongyan Liu, Michael Dahl, Ji. Bong Joo, Na Li, Lianjun Wang, Yadong Yin, Thermal synthesis of silver nanoplates revisited: a modified photochemical process, ACS Nano 10 (2014) 10252–10261.

[22] A. Peled, N. Mirchin, Liquid phase photodeposition processes from colloid solutions, in: A. Peled (Ed.), Photo-Excited Processes, Diagnostics and Applications, Springer, Boston, MA, 2003.

[23] I. Baal-Zedaka, S. Hava, N. Mirchin, R. Margolin, M. Zagon, I. Lapsker, J. Azoulay, A.Z. Peled, Photodeposition of optical elements from colloid solutions, Colloids Surf. A Physicochem Eng. Asp. 217 (2003) 191–202.

[24] E. Albiter, M.A. Valenzuela, S. Alfaro, G. Valverde-Aguilar, F.M. Martínez-Pallares, Photocatalytic deposition of Ag nanoparticles on TiO$_2$: metal precursor effect on the structural and photoactivity properties, J. Saudi Chem. Soc. 19 (2015) 563–573.

[25] Kasper Wenderich, Guido Mul, Methods, mechanism and applications of photodeposition in photocatalysis: a review, Chem. Rev. 116 (2016) 14587–14619.

[26] M. Sakamoto, M. Fujistuka, T. Majima, Light as a construction tool of metal nanoparticles: synthesis and mechanism, J. Photochem. Photobiol. C (2009) 33–56.

[27] Julia L. Rodríguez, Miguel A. Valenzuela, Hugo Tiznado, Tatiana Poznyak, Evelyn Flores, Synthesis of nickel oxide nanoparticles supported on SiO$_2$ by sensitized liquid phase photodeposition for applications in catalytic ozonation, J. Mol. Catal. A: Chem. 392 (2014) 39–49.

[28] S. Scirè, S. Giuffrida, C. Crisafulli, P.M. Riccobene, A. Pistone, Liquid phase photodeposition in the presence of unmodified β-cyclodextrin: a new approach for the preparation of supported Pd catalysts, J. Mol. Catal. A: Chem. 353 (2012) 87–94.

[29] S. Scirè, C. Crisafulli, S. Giuffrida, G. Ventimiglia, C. Bongiorno, C. Spinella, Preparation of ceria and titania supported Pt catalysts through liquid phase photodeposition, J. Mol. Catal. A: Chem. 333 (2010) 100–108.

[30] Bo-En Wu, Chia-Ying Chiang, Photochemical metal organic deposition of FeO$_x$ catalyst on BiVO$_4$ for improving solar-driven water oxidation efficiency, J. Taiwan Inst. Chem. Eng. 80 (2017) 1014–1021.

[31] Hamidreza Hoshyarmanesh, Mojtaba Ghodsi, Hyung-Ho Park, Electrical properties of UV-irradiated thick film piezo-sensors on superalloy IN718 using photochemical metal organic deposition, Thin Solid Films 616 (2016) 673–679.

[32] G.E. Buono-Core, A.H. Klahn, C. Castillo, E. Muñoz, C. Manzur, G. Cabello, B. Chornik, Synthesis and characterization of thin molybdenum oxide films prepared from molybdenum dioxo tropolonate precursors by photochemical metal-organic deposition (PMOD) and its evaluation as ammonia gas sensors, J. Non-Cryst. Solids 387 (2014) 21–27.

[33] G. Cabello, L. Lillo, C. Caro, M. Seguel, G.E. Buono-Core, Y. Huentupil, B. Chornik, C. Carrasco, C.A. Rodríguez, Synthesis, characterization and optical properties of ATiO$_3$–Pr thin films prepared by a photochemical method (where A = Ba and Ca), Mater. Res. Bull. 70 (2015) 32–39.

[34] G. Cabello-Guzman, L. Lillo-Arroyo, C. Caro-Díaz, F. Valenzuela-Melgarejo, A. Fernandez-Perez, G.E. Buono-Core, B. Chornik, Study on the photochemical preparation of nickel gallium oxide spinel doped with Eu(III) ions from carboxylate and β-diketonate complexes and the evaluation of its optical properties, Thin Solid Films 647 (2018) 33–39.

[35] W.L. Law, R.H. Hill, Synthesis and characterization of photochemically produced thin films of CeO$_2$ films by photoresist-free lithography, Mater. Res. Bull. 1 (1998) 69–80.

[36] W.L. Law, Ross H. Hill, Photolitographic deposition of insulating Al$_2$O$_3$ films from thin amorphous films of aluminum complexes on silicon surfaces, Thin Solid Films 375 (2000) 42–45.

[37] Hyeong-Ho Park, Tae-Jung Ha, Hyung-Ho Park, Tae Song Kim, Ross H. Hill, Effects of UV-irradiation during photochemical metal-organic deposition on the electric and ferroelectric properties of direct-patternable Bi$_{3.25}$La$_{0.75}$Ti$_3$O$_{12}$ films, Mater. Lett. 62 (2008) 4143–4145.

[38] G.E. Buono-Core, A.H. Klahn, G. Cabello, L. Lillo, Characterization of amorphous Pt/ZnO films grown on silicon(100) substrates by a photochemical metal organic deposition and their potential use as gas sensors, Polyhedron 62 (2013) 1–6.

[39] Simon Trudel, Colin H.W. Jones, Ross H. Hill, Magnetic properties of nanocrystalline iron oxide/amorphous manganese oxide nanocomposite thin films prepared via

photochemical metal-organic deposition, J. Mater. Chem. 17 (2007) 2206–2218.

[40] G. Cabello, L. Lillo, C. Caro, G.E. Buono-Core, B. Chornik, M.A. Soto, Structure and optical characterization of photochemically prepared ZrO$_2$ thin films doped with erbium and europium, J. Non-Cryst. Solids 354 (2008) 3919–3928.

[41] G. Cabello, L. Lillo, C. Caro, M. Seguel, C. Sandoval, G.E. Buono-Core, B. Chornik, M. Flores, A photochemical proposal for the preparation of ZnAl$_2$O$_4$ and MgAl$_2$O$_4$ thin films from b-diketonate complex precursors, Mater. Res. Bull. 77 (2016) 212–220.

[42] Salvatore Giuffrida, Lucia Laura Costanzo, Guglielmo Guido Condorelli, Giorgio Ventimiglia, Ignazio Luciano Fragala, Photochemistry of bis(1,1,1,5,5,5-hexafluoro-2,4 pentanedionato)strontium tetraglyme solutions for eventual liquid phase photochemical deposition, Inorg. Chim. Acta 358 (2005) 1873–1881.

[43] Guglielmo G. Salvatore Giuffrida, Lucia L. Condorelli, Ignazio L. Costanzo, Giorgio Fragala, Ventimiglia, Graziella Vecchio, Photochemical mechanism of the formation of nanometer-sized copper by UV irradiation of ethanol Bis(2,4-pentan-dionato)copper(II) solutions, Chem. Mater. 16 (2004) 1260–1266.

[44] Mustafa Aghazadeh, Taher Yousefi, Mehdi Ghaemi, Low-temperature electro-chemical synthesis and characterization of ultrafine Y(OH)$_3$ and Y$_2$O$_3$ nano-particles, J. Rare Earth 3 (2012) 236–240.

[45] Christopher T. Hai Du, Armin D. Williams, Ebner, James A. Ritter, In situ FTIR spectroscopic analysis of carbonate transformations during adsorption and deso-rption of CO$_2$ in K-promoted HTlc, Chem. Mater. 22 (2010) 3519–3526.

[46] Junying Zhang, Zhongtai Zhang, Zilong Tang, Yuanhua Lin, Zishan Zheng, Luminescent properties of Y$_2$O$_3$:Eu synthesized by sol–gel processing, J. Mater. Process. Technol. 121 (2002) 265–268.

[47] Jiaqi Zhu, Yuankun Zhu, Weixia Shen, Yongjie Wang, Jiecai Han, Gui Tian, Pei Lei, Bing Dai, Growth and characterization of yttrium oxide films by reactive magnetron sputtering, Thin Solid Films 519 (2011) 4894–4898.

[48] S.A. Barve, Jagannath, N. Mithal, M.N. Deo, N. Chand, B.M. Bhanage, L.M. Gantayet, D.S. Patil, Microwave ECR plasma CVD of cubic Y$_2$O$_3$ coatings and their characterization, Surf. Coat. Technol. 204 (2010) 3167–3172.

[49] J.-C. Dupin, D. Gonbeau, P. Vinatier, A. Levasseur, Systematic XPS studies of metal oxides, hydroxides and peroxides, Phys. Chem. Chem. Phys. 2 (2002) 1319–1324.

[50] Hee Jung Yoon, Jisuk Lee, Young-Il Kim, Dae Won Cho, Youngku Sohn, Synthesis and characterization of Er$_2$O$_3$ nanorods and nanosheets, Ceram. Int. 43 (2017) 2069–2075.

[51] Sohn Youngku, Yb$_2$O$_3$ nanowires, nanorods and nano-square plates, Ceram. Int. 44 (2018) 3341–3347.

[52] R. Hari Krishna, B.M. Nagabhushana, H. Nagabhushana, R.P.S. Chakradhar, R. Sivaramakrishna, C. Shivakumara, Tiju Thomas, Auto-ignition based synthesis of Y$_2$O$_3$ for photo- and thermo-luminescent applications, J. Alloy. Compd. 585 (2014) 129–137.

[53] A. Siaï, K. Horchani-Naifer, P. Haro-González, M. Férid, Effect of ytterbium sub-stitution on LaEr$_{(1-x)}$Yb$_x$O$_3$ optical properties, J. Lumin. 172 (2016) 65–70.

[54] R. Hari Krishna, B.M. Nagabhushana, H. Nagabhushana, R.P.S. Chakradhar, R. Sivaramakrishna, C. Shivakumara, Tiju Thomas, Auto-ignition based synthesis of Y$_2$O$_3$ for photo- and thermo-luminescent applications, J. Alloy. Compd. 585 (2014) 129–137.

[55] Qiao Yanmin, Guo Hai, Upconversion properties of Y$_2$O$_3$:Er films prepared by sol-gel method, J. Rare Earth 3 (2009) 406–410.

[56] Qing Lu, Qiuhong Yang, Ye Yuan, Cen Jiang, Yonggang Wang, Fabrication and luminescence properties of Er^{3+} doped yttrium lanthanum oxide transparent ceramics, Ceram. Int. 40 (2014) 7367–7372.

[57] Edita Garskaite, Mikael Lindgren, Mari-Ann Einarsrud, Tor Grande, Luminescent properties of rare earth (Er, Yb) doped yttrium aluminium garnet thin films and bulk samples synthesised by an aqueous sol–gel technique, J. Eur. Ceram. Soc. 30 (2010) 1707–1715.

[58] Yaxin Guo, Jie Wei, Yalong Liu, Tiantian Yang, Zhuo Xu, Surfactant-tuned phase crystallinity and morphologies of NaYF$_4$:Yb^{3+}·Er^{3+} hexagonal microstructures and their photoluminescence properties, J. Mater. Sci: Mater. Electron 29 (2018) 2463–2470.

[59] Yue Liu, Dan Li, Qianli Ma, Wensheng Yu, Xue Xi, Xiangting Dong, Jinxian Wang, Guixia Liu, Fabrication of novel Ba$_4$Y$_3$F$_{17}$:Er^{3+} nanofibers with upconversion fluorescence via combination of electrospinning with fluorination, J. Mater. Sci: Mater. Electron 27 (2016) 11666–11673.